System-wide organization of actin cytoskeleton determines organelle transport in hypocotyl plant cells

David Breuer[a,b,1], Jacqueline Nowak[a,b,c], Alexander Ivakov[c,d], Marc Somssich[c], Staffan Persson[c,e,2], and Zoran Nikoloski[a,b,2]

[a]Systems Biology and Mathematical Modeling, Max Planck Institute of Molecular Plant Physiology, 14476 Potsdam, Germany; [b]Bioinformatics, Institute of Biochemistry and Biology, University of Potsdam, 14476 Potsdam, Germany; [c]School of Biosciences, University of Melbourne, Parkville, VIC 3010, Australia; [d]ARC Centre of Excellence for Translational Photosynthesis, College of Medicine, Biology and Environment, Australian National University, Canberra, Acton, ACT 2601, Australia; and [e]Plant Cell Walls, Max Planck Institute of Molecular Plant Physiology, 14476 Potsdam, Germany

Edited by Natasha V. Raikhel, Center for Plant Cell Biology, Riverside, CA, and approved May 25, 2017 (received for review April 26, 2017)

The actin cytoskeleton is an essential intracellular filamentous structure that underpins cellular transport and cytoplasmic streaming in plant cells. However, the system-level properties of actin-based cellular trafficking remain tenuous, largely due to the inability to quantify key features of the actin cytoskeleton. Here, we developed an automated image-based, network-driven framework to accurately segment and quantify actin cytoskeletal structures and Golgi transport. We show that the actin cytoskeleton in both growing and elongated hypocotyl cells has structural properties facilitating efficient transport. Our findings suggest that the erratic movement of Golgi is a stable cellular phenomenon that might optimize distribution efficiency of cell material. Moreover, we demonstrate that Golgi transport in hypocotyl cells can be accurately predicted from the actin network topology alone. Thus, our framework provides quantitative evidence for system-wide coordination of cellular transport in plant cells and can be readily applied to investigate cytoskeletal organization and transport in other organisms.

actin | cytoskeleton | Golgi | image processing | networks

The cell interior is a heterogeneous and crowded space comprising a large range of molecules and organelles (1, 2). Because diffusion through this complex environment is not sufficient to match varying demands for cell maintenance and growth, intricate cellular transport schemes have evolved (3, 4). Transport of cellular components across large distances relies substantially on the cytoskeleton (4–7). Moreover, in plant cells, many organelles move rapidly due to actomyosin-based cytoplasmic streaming (8–10). For instance, Golgi transport relies on the actomyosin system, and an impaired actin cytoskeleton leads to Golgi aggregation and reduced secretion and endocytosis (10–12). Although many molecular features of actin-based transport in plant cells have been elucidated (13, 14), quantitative measures of the structure of the actin cytoskeleton, and how this structure relates to organelle transport, remain elusive. This is largely due to the difficulties in accurately segmenting the actin cytoskeleton and organelle movement, in particular in growing plant cells.

Theoretical models have been used to analyze the interplay between cytoplasmic streaming and actin organization, demonstrating the emergence of self-organized, rotational streaming patterns (3, 15). However, these studies neglected the discrete, filamentous structure of the cytoskeleton. Theoretical investigations that have considered discrete cytoskeletal structures revealed different regimes of transport, depending on the contribution from diffusion or motor-protein–driven transport along random networks of segments (16); the impact of motor-protein movements on cytoplasm in lattice networks (17); and the effect of length, orientation, and polarity of random filament segments on transport rates (18). The studies that do incorporate biological data have suggested that plant cytoskeletal networks, approximated as grids, may support efficient transport processes in hypocotyl cells (19, 20) and that organelle movement depends on local actin structures in root epidermal cells (10). A detailed study of leaf trichome growth demonstrated the importance of organized actin networks for efficient and targeted distribution of new cell wall material (21). However, a global, system-wide view of actin-based organelle transport remains elusive and is complicated by differences between cell types and developmental stages.

Here, we developed a network-based framework that accurately segments the actin cytoskeleton from three developmental stages of hypocotyl plant cells and combined it with an automated tracking of Golgi transport. This approach allowed us to analyze the four aspects of the actin cytoskeletal transport system, including its structure, design principles, dynamics, and control (22). We found that the actin cytoskeleton maintains properties that support efficient transport over time in growing, partially and fully elongated hypocotyl cells, despite rapid reorganization. We also show that Golgi wiggling behavior is reminiscent of

Significance

In the crowded interior of a cell, diffusion alone is insufficient to master varying transport requirements for cell sustenance and growth. The dynamic actin cytoskeleton is an essential cellular component that provides transport and cytoplasmic streaming in plant cells, but little is known about its system-level organization. Here, we resolve key challenges in understanding system-level actin-based transport. We present an automated image-based, network-driven framework that accurately incorporates both actin cytoskeleton and organelle trafficking. We demonstrate that actin cytoskeleton network properties support efficient transport in both growing and elongated hypocotyl cells. We show that organelle transport can be predicted from the system-wide cellular organization of the actin cytoskeleton. Our framework can be readily applied to investigate cytoskeleton-based transport in other organisms.

Author contributions: D.B., S.P., and Z.N. designed research; D.B. and J.N. performed research; D.B., J.N., and M.S. contributed new reagents/analytic tools; D.B. and J.N. analyzed data; D.B., J.N., A.I., S.P., and Z.N. wrote the paper; and A.I. and M.S. recorded data.

The authors declare no conflict of interest.

This article is a PNAS Direct Submission.

Freely available online through the PNAS open access option.

[1]To whom correspondence should be addressed. Email: breuer@mpimp-golm.mpg.de.

[2]S.P. and Z.N. contributed equally to this work.

This article contains supporting information online at www.pnas.org/lookup/suppl/doi:10.1073/pnas.1706711114/-/DCSupplemental.

optimized search strategies that might indicate efficient uptake and deposition of Golgi-related cell material. In addition, we demonstrated that features of Golgi transport can be predicted from properties of the system-wide organization of the actin cytoskeleton. Altogether, our framework opens up a systems perspective to dissect and understand the transport functionality of the actin cytoskeleton.

Results

A Pipeline to Extract and Represent the Actin Cytoskeleton as a Network. Because the actin cytoskeleton is composed of discrete and interconnected filaments, it can be efficiently represented in a network-based framework (19, 23, 24) with nodes representing crossings or end points of actin filaments (AFs) and weighted edges capturing AF segments. We extracted network representations from partially elongated *Arabidopsis thaliana* (*Arabidopsis*) hypocotyl cells, around $3\,\mathrm{mm}$ from the apical hook, that expressed FABD-GFP, using spinning-disc confocal microscopy data (Fig. 1*F* for pipeline; *Materials and Methods*). To study actin-based transport at different cell developmental stages, we further analyzed fully elongated as well as growing hypocotyl cells, around $5\,\mathrm{mm}$ and $1\,\mathrm{mm}$ from the apical hook, respectively (Fig. S1 and below). The recorded images were corrected for drift and bleaching (Fig. 1*A*), manually cropped to the cellular region of interest, and filtered to enhance tube-like structures of the cytoskeleton with a parameter v_{width} (Fig. 1*B*). AFs were segmented by applying an adaptive median threshold of block size, v_{thres} (Fig. 1*C*). The binary images were skeletonized to obtain AF center lines and spurious fragments smaller than v_{size} pixels or below v_{int} of the average fragment intensity were removed (Fig. 1*D*). Networks were obtained by identifying the nodes, adding edges between pairs of nodes directly connected via the skeleton, and assigning edge weights reflecting features of AF segments, e.g., average thickness (Fig. 1*E*).

To test whether our network-based framework captured relevant biological features of the actin cytoskeleton, we compared our automated segmentations against synthetic images of known cytoskeleton-like structures (Fig. 1*G*) as well as manually segmented cytoskeleton images as a gold standard (Fig. 1*H*). Because the accuracy of the network representation relies

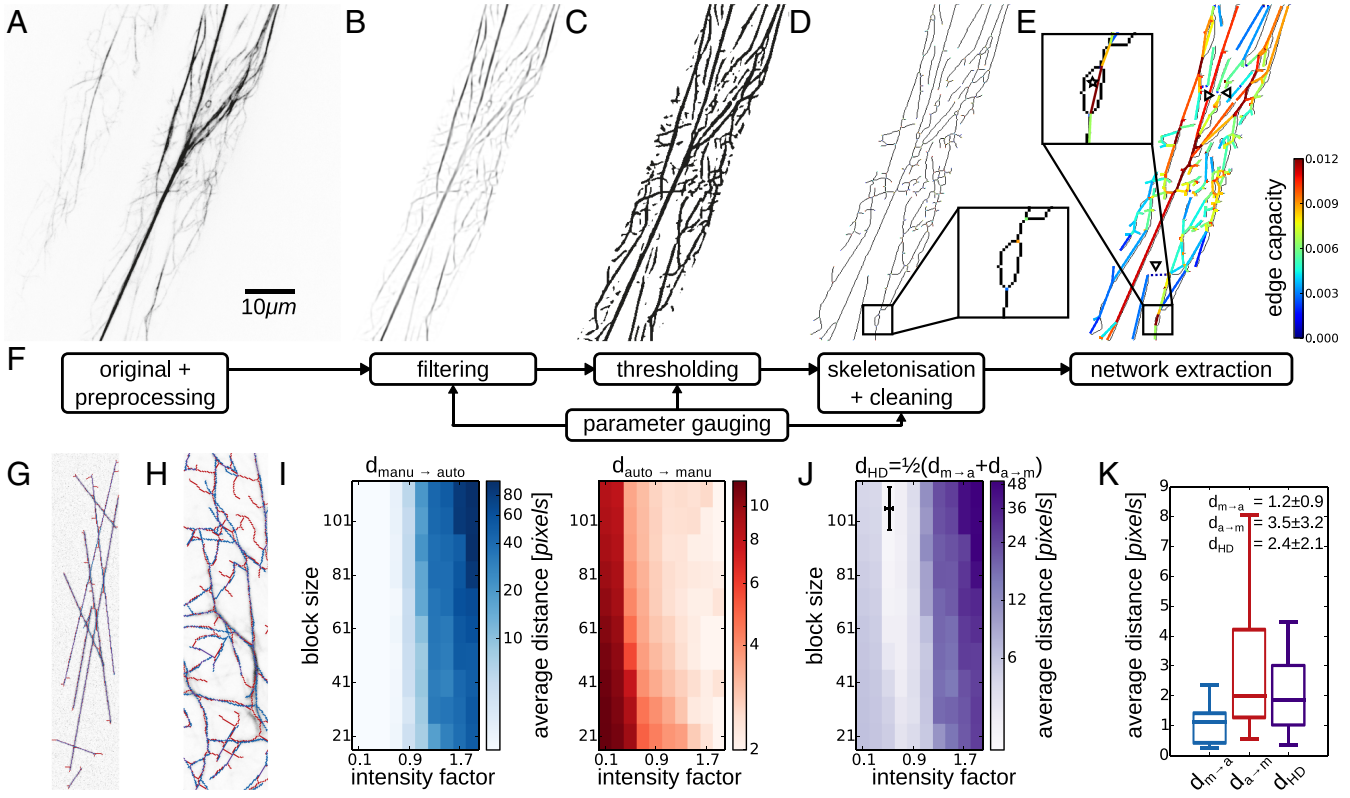

Fig. 1. Automated extraction and validation of networks from actin cytoskeletal image data. (*A*) Grayscale confocal image of two partially elongated *Arabidopsis* hypocotyl cells after registration and background subtraction ("original + preprocessing"). The same cell was used as example throughout the paper. (*B*) Cytoskeleton image with improved signal-to-noise ratio after cropping of the largest cell and application of tubeness filter ($v_{\mathrm{width}} = 1.8$; "filtering"). (*C*) Binary cytoskeleton image after application of adaptive median threshold ($v_{\mathrm{thres}} = 101$; "thresholding"). (*D*) Skeletonized cytoskeletal structures after removal of spurious fragments of small size or low intensity ($v_{\mathrm{size}} = 27$ pixels and $v_{\mathrm{int}} = 0.5$; "skeletonization + cleaning"). Positions of network nodes are marked by colored pixels (*Inset*). (*E*) Overlay of skeleton image and extracted cytoskeletal network with edges color coded by their capacity, reflecting average filament thickness ("network extraction"). Multiple filaments may contribute to an edge (compare *Inset* and star). Edges were added to connect the network (compare dotted lines and triangles). (*F*) Overview of automated pipeline for network-based representation of the actin cytoskeleton incorporating image processing (*A*–*D*), network extraction (*E*), and parameter gauging (*G*–*K*). (*G*) Overlay of synthetic filaments (blue) and automated segmentation (red) of a synthetic cytoskeleton image (gray). (*H*) Overlay of manual (blue) and automated (red) segmentation of a biological cytoskeleton image (gray). (*I*) Four image processing parameters were varied to determine their optimal values for 20 images and 20 images of synthetic and biological cytoskeletons, respectively, which were segmented manually for comparison ("parameter gauging"). Segmentation quality was measured by the average of the smallest distance, $d_{\mathrm{manu}\to\mathrm{auto}}$ (blue), from the pixels of the manual segmentation to those of the automated segmentation and vice versa, $d_{\mathrm{auto}\to\mathrm{manu}}$ (red). Shown are sections of the parameter space, averaged over all 40 studied images, for fixed $(v_{\mathrm{width}}, v_{\mathrm{int}}) = (1.8, 101)$ and varying block size v_{thres} and size threshold v_{size}. (*J*) Minimization of the Haussdorf distance $d_{\mathrm{HD}} = \frac{1}{2}\,(d_{\mathrm{manu}\to\mathrm{auto}} + d_{\mathrm{auto}\to\mathrm{manu}})$ (purple) to avoid both over- and undersegmentation yielded $(v^*_{\mathrm{width}}, v^*_{\mathrm{thres}}, v^*_{\mathrm{size}}, v^*_{\mathrm{int}}) = (1.8, 101, 27, 0.50) \pm (0.2, 8.0, 8.9, 0.06)$ (mean ± SD). (*K*) Distribution of average distances between manual and automated segmentations for the optimal parameters with $d_{\mathrm{manu}\to\mathrm{auto}} = 1.2 \pm 0.9$ pixels, $d_{\mathrm{auto}\to\mathrm{manu}} = 3.5 \pm 3.2$ pixels, and $d_{\mathrm{HD}} = 2.4 \pm 2.1$ pixels, respectively.

on four parameters (v_{width}, v_{thres}, v_{size}, and v_{int}), we performed extensive gauging by varying these parameters in a wide range of values (Fig. 1 *I* and *J*) and identified those ensuring best agreement between manual and automated segmentations measured by the Haussdorf distance, i.e., the average minimum distance between pixels of the two segmentations (25, 26). Parameter gauging yielded an optimal average of $d_{\mathrm{HD}} = 2.4 \pm 2.1$ pixels (Fig. 1 *J* and *K*; mean $\pm$ SD), comparable to contending approaches (*SI Materials and Methods*). Thus, whereas errors in the automated segmentation occur, our parameter optimization ensures an optimal compromise between over- and undersegmentation across different recordings.

Our approach is directly applicable to 3D image data. However, our focus in the main text on 2D networks is justified by the cylindrical shell geometry of the cortical cytoskeleton (19, 27) as well as the size of the transported Golgi, which may bridge gaps between cortical AFs that are not resolved in 2D images (28–30). Moreover, we show that our findings remain valid for 3D image data (Fig. S2 and below). Thus, our approach yields an accurate and mathematically powerful network representation of the cytoskeleton in hypocotyl plant cells from image data.

The Network Representations Capture Biologically Relevant Features of the Actin Cytoskeleton. To ensure that our framework captured known changes in the actin cytoskeleton, we determined differences in cytoskeletal organization between partially elongated hypocotyl cells of plants treated with Latrunculin B (LatB; Fig. 2*A*), a drug that inhibits actin polymerization (31), and control cells (Fig. 2*B*; seven cells from seven different seedlings per treatment). To quantify actin network phenotypes, we computed the number of connected components after removal of edges with capacities below the 50th percentile as a measure of fragmentation (Fig. 2*D* and ref. 32; mathematical definitions and interpretations of all studied network properties are given in Table S1). Fragmentation was lower in networks of control than of LatB-treated cells (Fig. 2*E*; independent two-sample t test P value $P_t < 10^{-50}$), indicating that large connected patches of AFs were absent in LatB-treated cells, consistent with visual inspection. Similarly, the average edge capacity was higher in control than in LatB-treated cells ($P_t < 10^{-38}$), reflecting a reduction in actin bundling in the LatB-treated cells. Finally, these findings were corroborated by the assortativity (32), which quantifies whether two adjacent nodes are of similar degree and reflects the network heterogeneity. We found stronger heterogeneity for control than for LatB-treated cells ($P_t < 10^{-50}$), suggesting regions of bundled actin that are surrounded by AFs in the control cells.

To further assess the filamentous structure of the actin cytoskeleton, we compared the arc length of filament segments to their Euclidean length and found a strong correlation (Fig. 2*F*; Pearson correlation coefficient $c_P = 0.998$ and P value $P_P < 10^{-50}$). Consequently, filament bending, i.e., the ratio of the two lengths, was small, $B = 1.2 \pm 0.2$, in particular for long filament segments (Fig. 2*F*, *Inset*). This limited bending of longer filament segments is plausible because actin bundles, typically resulting in longer filament segments, exhibit greater stiffness compared with AFs (33, 34). Furthermore, we found that filament segments were preferentially oriented in parallel to the major cell axis in control cells, but not in LatB-treated cells (Fig. 2*G*). To demonstrate the robustness of our findings, we showed that the differences in network properties between control and treatment were not affected by removal of a random fraction of edges, simulating effects of erroneous network extraction (Fig. S3).

Next, we compared cytoskeletal networks in hypocotyl cells at different developmental stages, i.e., in growing and fully elongated cells, and found notable differences (Fig. S1). In particular, in contrast to both partially and fully elongated hypocotyl cells, the actin cytoskeleton in untreated growing hypocotyl cells showed stronger fragmentation and weaker bundling than in their LatB-treated counterparts. These differences are in agreement with the more even distribution and more strongly branched structure of the actin cytoskeleton in growing hypocotyl cells (35, 36) (Fig. S1), as well as the continuous gradient in cell elongation rates along the hypocotyl in dark-grown *Arabidopsis* seedlings (37). Moreover, our findings from 2D image data were corroborated by analyses of 3D image data and networks (Fig. S2). Therefore, our results show that the extracted network representations of the actin cytoskeleton enable automated phenotyping of cytoskeletal structures.

The Actin Cytoskeleton Supports Efficient Transport. A major function of the plant actin cytoskeleton is to mediate transport of a range of organelles and compartments. To assess the transport efficiency of actin networks in partially elongated hypocotyl cells, we computed a number of seminal network properties and compared them against ensembles of two types of randomized null model networks (each network was randomized 20 times; Fig. 2*C* for first null model that shuffles node positions and edges and Fig. S3 for second null model that shuffles edge properties only). We determined the average path length (32), which reflects the reachability of a network, and compared it against an ensemble of networks from the first null model (Fig. 2*H*). We found that the average path length of the extracted networks was smaller than that of the null model networks (Fig. 2*I*; $P_t < 10^{-50}$; Fig. S3 for analysis of robustness of this finding against removal of edges). This difference indicates that the actin cytoskeleton is tuned toward shorter path lengths. Similarly, the coefficients of variation (CVs) of the shortest path lengths in the extracted networks were smaller than expected from the null model networks ($P_t < 10^{-50}$), indicating that also fluctuations in the path length between any two nodes are maintained at a low level. Another classical transport-related network property is the algebraic connectivity (32), which reflects the redundancy of paths between any two nodes and thus captures the robustness of the transportation network against disruptions. The algebraic connectivity of the extracted networks was higher than expected by chance ($P_t < 10^{-14}$). In contrast, the LatB-disrupted actin cytoskeletons did not show any significant differences in their transport-related network properties compared with the null model networks (Fig. S3). These findings support the hypothesis that transport efficiency is a biological design principle of the intact actin cytoskeleton (19).

To investigate the structural origin of this transport efficiency, we reconsidered the assortativity (32) of the cytoskeleton and found that it was higher in the extracted networks than expected by chance ($P_t < 10^{-50}$). Similarly, we found that the CV of the angles between AF segments and the major cell axis was smaller in the extracted networks than expected by chance ($P_t < 10^{-50}$). Together these findings suggest that the formation of connected patches of aligned actin bundles is a functionally relevant feature of the cytoskeleton.

To ensure that our results were robust, we used an additional and more restricted null model, which shuffles only edge properties. Whereas the first null model is more flexible, the second one excludes potential artifacts that could arise from an increased number of edge crossings or a more homogeneous distribution of node positions compared with the extracted networks (Fig. S3). Our findings from the first null model were consistently confirmed by the second one. Hence, differences in the studied network properties between extracted and null model networks are not an artifact of the randomization procedures.

Despite organizational differences of the actin cytoskeleton in hypocotyl cells at different developmental stages, the actin network in partially elongated as well as fully elongated and growing hypocotyl cells showed properties of efficient transport (Fig. S1). For example, both reachability and robustness of the actin networks were better than expected by chance. Again, our findings

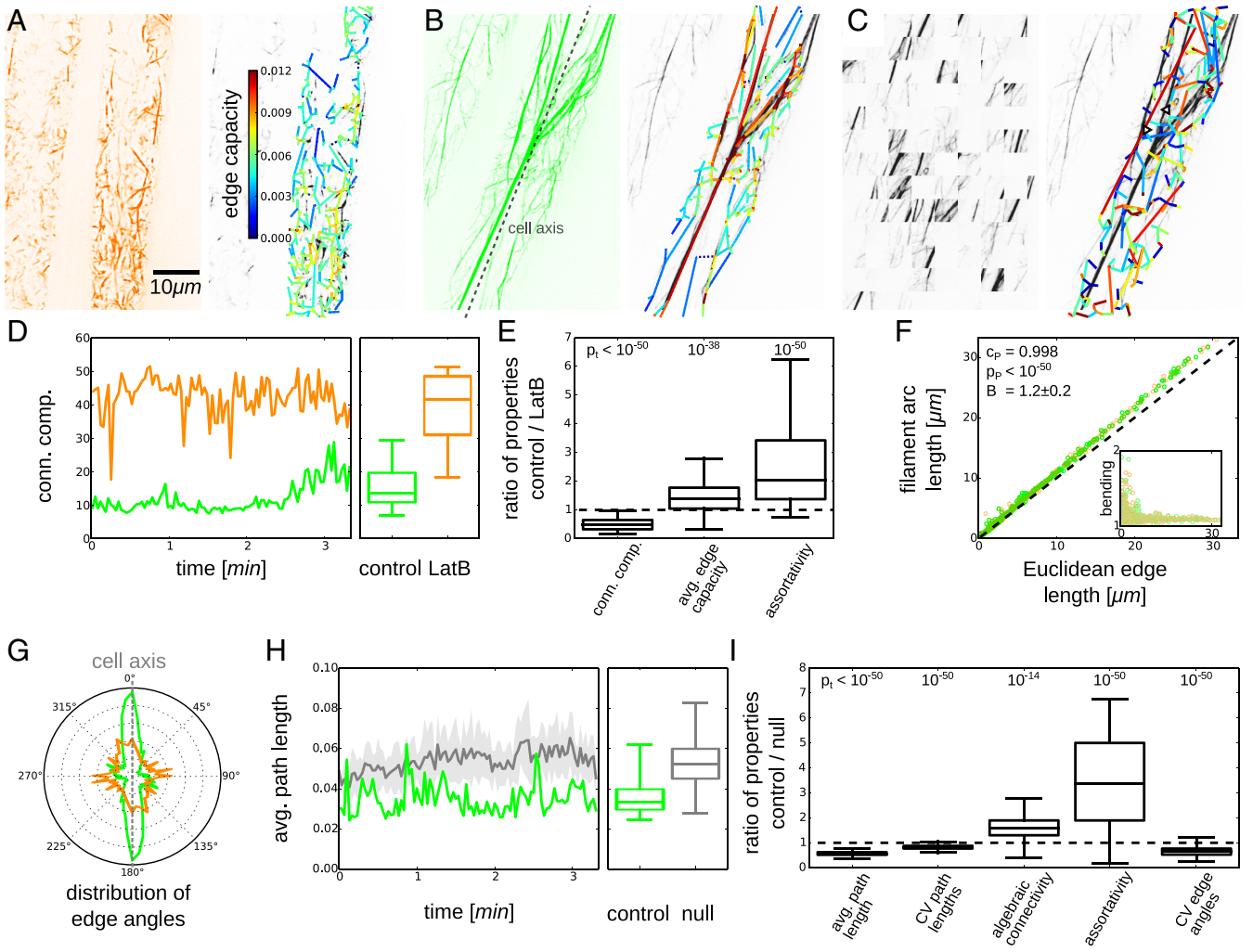

Fig. 2. Phenotyping of actin cytoskeleton using the extracted networks captures biological signals and reveals transport efficiency. Shown are results for partially elongated hypocotyl cells of plants treated with the actin-disrupting drug LatB (orange), untreated control plants (green), and ensembles of 20 randomized networks (gray). (*A*) Cellular recording (*Left*) and extracted actin network (*Right*) of a LatB-treated cell with edge colors representing edge capacities. (*B*) Cellular recording (*Left*) and extracted actin network (*Right*) of an untreated control cell. (*C*) Artistic interpretation of the randomization procedure (*Left*) and a randomized network (*Right*) of the control cell (*B*) with occasional edge crossings (e.g., triangles). (*D*) Time series and box plots of the number of connected components after removal of edges with capacities below the 50th percentile ("fragmentation") for a control and a LatB-treated cell. (*E*) Ratios of different properties of networks extracted from seven control and seven LatB-treated cells. The number of connected components was lower and the average edge capacity ("bundling") and the degree assortativity ("heterogeneity") were higher for control than for LatB-treated cells (independent two-sample *t* test *P* values $P_t < 0.05$ were considered significant). (*F*) Scatter plots of the arc length a_F of the filament segments vs. the Euclidean length a_E of the corresponding edges showed strong correlation for control and LatB-treated cells (Pearson correlation coefficient $c_P = 0.998$ and *P* value $P_P < 10^{-50}$). *F*, *Inset* displays relative lengths $B = a_E^{-1} a_F$ ("bending") with an average of $B = 1.2 \pm 0.2$ (mean ± SD). (*G*) Distribution of edge angles, weighted by edge capacities, relative to the major cell axis showed a prevalence of AFs parallel to the cell axis in the control cells but not in LatB-treated cells. (*H*) Time series and box plots of the average path length ("reachability") for one control cell and 20 randomized networks of the first null model for each time step (mean ± SD). (*I*) The extracted actin networks of the seven control cells showed significantly lower average path lengths, CV of the path lengths ("dispersal"), and CV of the edge angles ("contortion") than their counterparts from the first null model. The algebraic connectivities ("robustness") and assortativities (heterogeneity) of the actin networks were higher than expected from the first null model.

remained valid when studying actin networks extracted from 3D image data (Fig. S2).

A potential issue, shared by all current approaches that extract transport-related networks from image data, is the unknown edge directionality. Individual AFs usually allow unidirectional movement of motor proteins only, and actin bundles in root hairs and other tip growing cells are typically composed of parallel AFs (9, 38, 39). In contrast, our analyses of cytoskeletal transport capacity rely on the assumption of bidirectional transport along edges. Indeed, our data showed that <50% of actin edges exhibit predominantly unidirectional movement of close-by Golgi, irrespective of the actin bundle thickness (see Fig. 4 and Fig. S4), partially justifying the assumption of bidirectional transport. This deviation from the expected unidirectional movement along bundles of parallel AFs may be partially due to noise-induced tracking errors that may lead to apparent bidirectional movement, especially during phases of Golgi pausing (11, 40). Moreover, in the computation of edge directionality a given Golgi may be associated with multiple edges and neighboring actin bundles may exhibit different orientations (10, 21) (details in Fig. S4). Finally, given the low Reynolds numbers of the cytoplasm (1), cytoplasmic streaming may carry temporarily detached Golgi (41) irrespective of the underlying actin bundle or its orientation (Fig. S5). In summary, our analyses indicate that transport efficiency

is a central design principle of the actin cytoskeleton in hypocotyl plant cells.

Automated Quantification of Golgi Movement. To quantify actin-based cellular transport, we studied partially elongated hypocotyl cells dually labeled with FABD-GFP and tdTomato-CesA6 (tdT-CesA6), used as a proxy for Golgi movement (42, 43). We analyzed the flow of Golgi through automated tracking (44, 45) in image series from control and LatB-treated cells (Fig. 3 *A* and *B*). Golgi bodies moved with velocity $v = 0.36 \pm 0.26\,\mathrm{s}^{-1}\cdot\mu\mathrm{m}$ in control cells (Fig. 3*C*), which is higher than $v = 0.04 \pm 0.03\,\mathrm{s}^{-1}\cdot\mu\mathrm{m}$ in LatB-treated cells, consistent with previous studies (10, 11). The Golgi movement was predominantly parallel to the major cell axis in control cells but not in LatB-treated cells (Fig. 3*D*), correlating with the orientation of actin bundles (compare with Fig. 2*G*). Thus, our automated tracking captures known features of Golgi movement and may therefore be suitable for further, more detailed analyses of Golgi behavior.

Golgi Bodies Exhibit Wiggling, Which Does Not Change Over Time or with Distance to the Actin Cytoskeleton. The movement of Golgi bodies is characterized as saltatory or stop and go (11, 30),

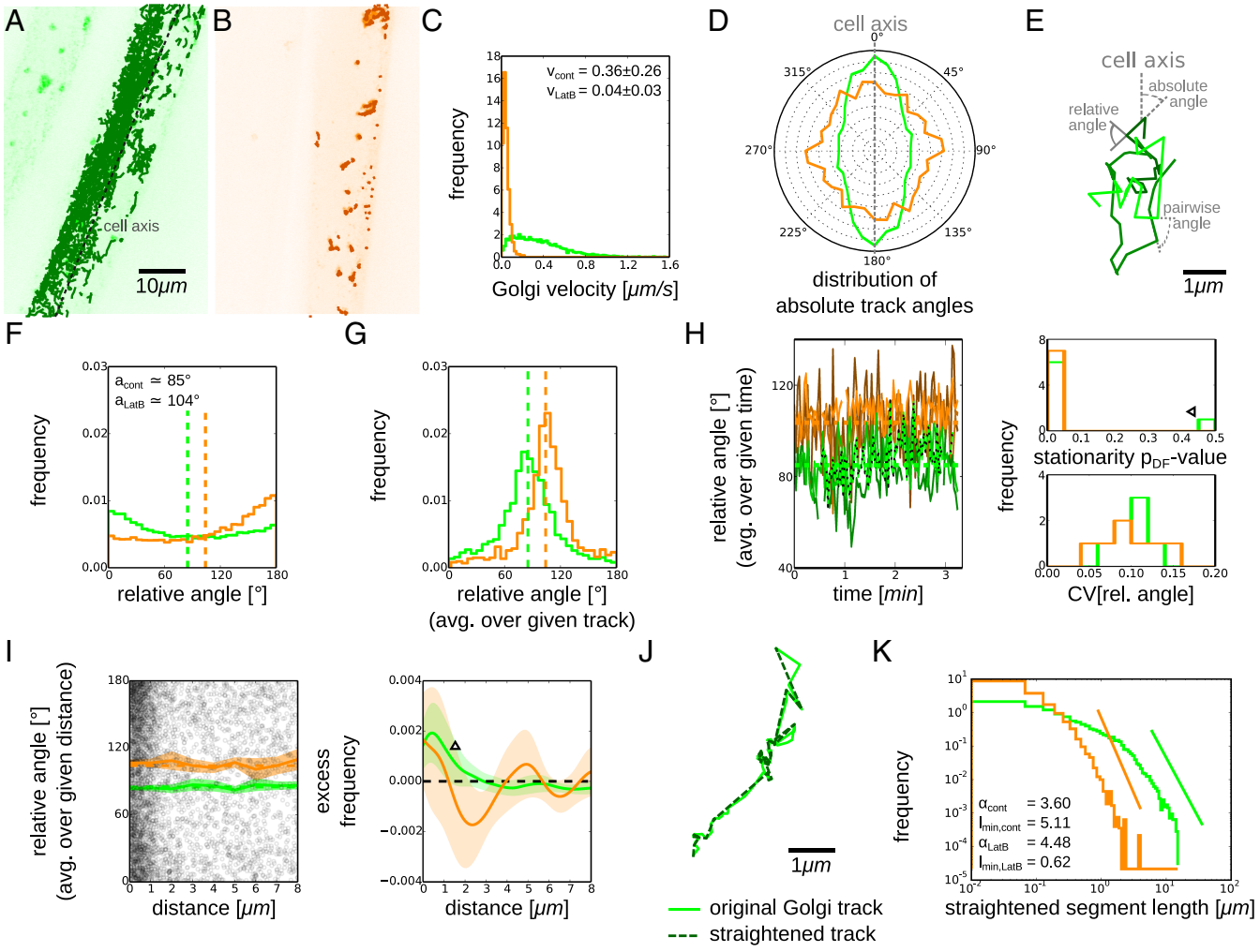

Fig. 3. Quantification of Golgi movement indicates stability and efficiency of wiggling behavior. Shown are Golgi dynamics in partially elongated hypocotyl cells of plants treated with the actin-disrupting drug LatB (orange) and untreated control plants (green). (*A*) Overlay of cellular recording of Golgi and Golgi tracks from a control cell. (*B*) Overlay of cellular recording of Golgi and Golgi tracks from a LatB-treated cell. (*C*) Distributions of Golgi velocities in LatB-treated cells, $v = 0.04 \pm 0.03\,\mathrm{s}^{-1}\cdot\mu\mathrm{m}$, and control cells, $v = 0.36 \pm 0.26\,\mathrm{s}^{-1}\cdot\mu\mathrm{m}$ (mean ± SD). (*D*) Distributions of absolute angles for control and LatB-treated cells. (*E*) Schematic of different angles used to study movement of Golgi bodies. Shown are the absolute angle between a Golgi track segment and the major cell axis (dashed gray angle) and the relative angle between two consecutive segments of a given Golgi track (solid gray angle), as well as the pairwise angle between two segments of two different Golgi tracks at a given time step (dotted gray angle). (*F*) Distributions of relative angles were broad with $a = 85° \pm 55°$ and $a = 104° \pm 55°$ for control and LatB-treated cells, respectively (dashed lines). (*G*) Distributions of relative angles, averaged over a given track, showed unimodal distributions with peaks around 85° and 104° for control and LatB-treated cells, respectively (dashed lines). (*H*) Time series of relative angles, averaged over a given time step, for each of the studied control and LatB-treated cells (*Left*). All time series were stationary; i.e., they showed no increasing or decreasing trend (*H*, *Upper Right*; augmented Dickey–Fuller unit root-test *P* values $P_{DF} < 0.05$), except one (see triangle). The fluctuations of the time series were small (*H*, *Lower Right*; CV [*a*] $= 0.10 \pm 0.03$). (*I*) Distributions of relative angles in dependence of distance of the track segments from the cytoskeleton (*Left*; circles show results for control cells; solid lines and shaded areas show mean ± SD). Excess of Golgi at a given distance from the cytoskeleton for control and LatB-treated cells (*I*, *Right*; compare solid lines and triangle) is given by the difference between the frequency of actual Golgi and the frequency of Golgi distributed randomly and uniformly across the cell area (dashed black line). (*J*) Example of an original Golgi track (solid light green) and the corresponding straightened track (dashed dark green), where each new track segment represents a largely straight run of the Golgi with relative angles below 90°. (*K*) Distributions of segment lengths of straightened Golgi tracks followed truncated power laws with exponents $\alpha = 3.60$ and $\alpha = 4.48$ and bounds $l_{min} = 5.11$ and $l_{min} = 0.62$ for control and LatB-treated cells, respectively.

whereby Golgi switch between periods of directed movement and undirected "wiggling" behavior (Fig. 3*E*). Whereas it has been suggested that Golgi wiggling is not specific to individual Golgi bodies (10), it is yet unclear whether Golgi wiggling changes over time or depends on the distance of the Golgi from the actin cytoskeleton. To quantify these characteristics, we computed the angles between consecutive Golgi track segments (referred to as "relative angles"; Fig. 3*E*) and refer to movement with relative angles above 90° as wiggling behavior (Fig. S6 shows another measure of wiggling). The observed distributions of relative angles across the studied cells were broad, demonstrating that both largely unidirectional movement and wiggling behavior were present (Fig. 3*F*). For LatB-treated cells, the average relative angle $a = 104^\circ \pm 55^\circ$ was larger than for control cells with $a = 85^\circ \pm 55^\circ$ and wiggling was thus more common. The distributions of relative angles averaged across a given track (Fig. 3*G*) peaked at around 90° for both untreated and LatB-treated cells, showing that the majority of Golgi tracks contained both periods of directed movement and wiggling behavior. Hence, our findings confirm that wiggling behavior is not specific to individual Golgi.

To test whether the prevalence of Golgi wiggling changes over time, we calculated the distribution of average relative angles over time (Fig. 3*H*, *Left*). We found that Golgi motility did not change during the course of the recordings (Fig. 3*H*, *Upper Right*). Moreover, the prevalence of Golgi wiggling showed only very minor fluctuations within and across time series (Fig. 3*H*, *Lower Right*; $\mathrm{CV}\,[a] = 0.10 \pm 0.03$), indicating that a constant fraction of Golgi exhibited wiggling behavior over time. Our data therefore suggest that Golgi wiggling is a common and stable cellular phenomenon. To study the effect of the distance between actin cytoskeleton and Golgi on wiggling, we computed the relative angles between consecutive track segments at a given distance from the cytoskeletal center line (Fig. 3*I*, *Left*). The frequency of Golgi was dependent on the distance to the AFs (Fig. 3*I*, *Right*), with high Golgi densities up to $2\,\mu\mathrm{m}$ from the AFs. Surprisingly, the prevalence of Golgi wiggling did not depend on the distance from the AFs (or on their thickness, Fig. S6). Moreover, although Golgi movement may vary substantially between cells, the features of Golgi movement studied here were highly consistent across cells (Fig. S6).

Movement Patterns of Golgi Resemble Search Strategies and Might Optimize Uptake and Delivery. We note that the Golgi wiggling resembles the searching behavior of foraging animals (46, 47) or microbial motion (48) that has been suggested to optimize search efficiency. This type of motion is characterized by random reorientations (Fig. 3*D*) and step sizes l that follow a power-law distribution $P(l) = \frac{\alpha-1}{l_{\min}}\left(\frac{l}{l_{\min}}\right)^{-\alpha}$. Because our image series provide snapshots with fixed time intervals, to quantify the distribution of Golgi step sizes, we considered track segments with relative angles below 90° as one step and replaced them by a single segment capturing the net displacement (Fig. 3*J*). Indeed, the distributions of step sizes of these straightened tracks followed truncated power laws with exponents $\alpha = 3.60$ and $\alpha = 4.48$ for control and LatB-treated cells, respectively [Fig. 3*K*; in particular, truncated power laws yielded higher likelihoods than exponential distributions (49)]. These exponents are larger than those typically reported for foraging animals or bacteria, $1 < \alpha < 3$ (46–48), but might indicate search strategies in small areas with a limited number of targets (50) or in the presence of obstacles or preferred areas (51–53), e.g., other organelles or delivery sites. Again, these findings were highly consistent across cells (Fig. S6).

Despite obvious differences in mechanisms underlying Golgi movement and animal foraging there may be similar goals. Namely, it is plausible that Golgi-derived material may need to be exchanged between parts of the plasma membrane, the endoplasmatic reticulum (ER), and other compartments. Assuming that these sites are not globally coordinated by the cell, the switching of Golgi between directed movement and wiggling behavior may therefore provide an efficient search strategy. This is compatible with proposed models of Golgi movement (30), such as the "vacuum cleaner" model (Golgi move through the cell and pick up products from the ER) or the "recruitment" model (Golgi pause in the vicinity of active ER sites to facilitate trafficking). Our findings might therefore indicate a connection between Golgi wiggling and the optimization of uptake and delivery of Golgi-related material throughout the cell.

The Golgi search behavior is compatible with the movement of Golgi along the actin structures. Whereas, at a given time step, the majority of Golgi stayed at the same AF, some faster Golgi moved to different AFs (Fig. S5). Moreover, it remains unclear whether Golgi bodies are transported through the cell by direct interactions with motor proteins or indirectly via cytoplasmic streaming (54). By investigating the relative movement of different Golgi at a given time step (referred to as "pairwise angles"; Fig. 3*E*), we found substantial antiparallel movement of close-by Golgi (Fig. S5). Taking into account the low Reynolds numbers of the cytoplasm (1), this antiparallel movement contradicts the assumption of indirect, cytoplasmic-streaming–induced movement and instead supports myosin-based transport of a substantial fraction of Golgi bodies. In conclusion, our data suggest that switching of Golgi to adjacent AFs is myosin dependent, whereas switching to nonadjacent AFs is due to cytoplasmic streaming that may carry the Golgi over large distances.

Local and Global Actin Network Architecture May Be Used to Predict Direction and Velocity of Golgi Movement. Our previous analyses assumed that the capacity of a given actin network edge, i.e., its average thickness, reflects its potential to transport cellular cargo (Fig. 2). To test this hypothesis, we studied the Golgi flow on two levels: First, we computed pairwise correlations between the properties of Golgi flow and actin structures, as modeled by our extracted networks. Second, we combined different edge properties of the actin networks to predict features of Golgi flow (e.g., direction and velocity), using a multiple–linear-regression approach. To this end, for the extracted actin networks (Fig. 4 *A* and *B*), we determined the local edge capacities and global edge properties that incorporate information about the importance of any given edge in the network context. Namely, we studied edge degree (measuring the total thickness of adjacent edges), the edge page rank (measuring the probability that cargo that randomly traverses the network is found at the given edge), the edge path betweenness (measuring the likelihood that the given edge lies on a shortest path through the network), and the edge flow betweenness [measuring the total maximum flow between any two nodes through the given edge (32); see Table S1 for mathematical definitions and explanations]. In parallel, from the Golgi tracks at each time step, we constructed an auxiliary Golgi flow network by copying the structure of the actin network and assigning new edge weights in the Golgi flow network according to various features of Golgi movement in the vicinity of the respective edge [e.g., the number of Golgi (Fig. 4*E*) or the direction and velocity of close-by Golgi (Fig. 4*F*)].

To investigate the relationship between actin structure and Golgi dynamics in partially elongated hypocotyl cells, we first computed the correlation between the determined edge properties of actin and Golgi flow networks. For instance, we studied the dependence of the Golgi direction and velocity on the actin edge rank. The correlation between the two properties varied over time and across cells (Fig. 4*G*). Across all studied partially elongated cells, this correlation was significant for control cells with $c_P = 0.384$, whereas no significant correlation was found for the LatB-treated cells with $c_P = -0.023$. These findings are compatible with the severely reduced flow (Fig. 3*C*) and increased

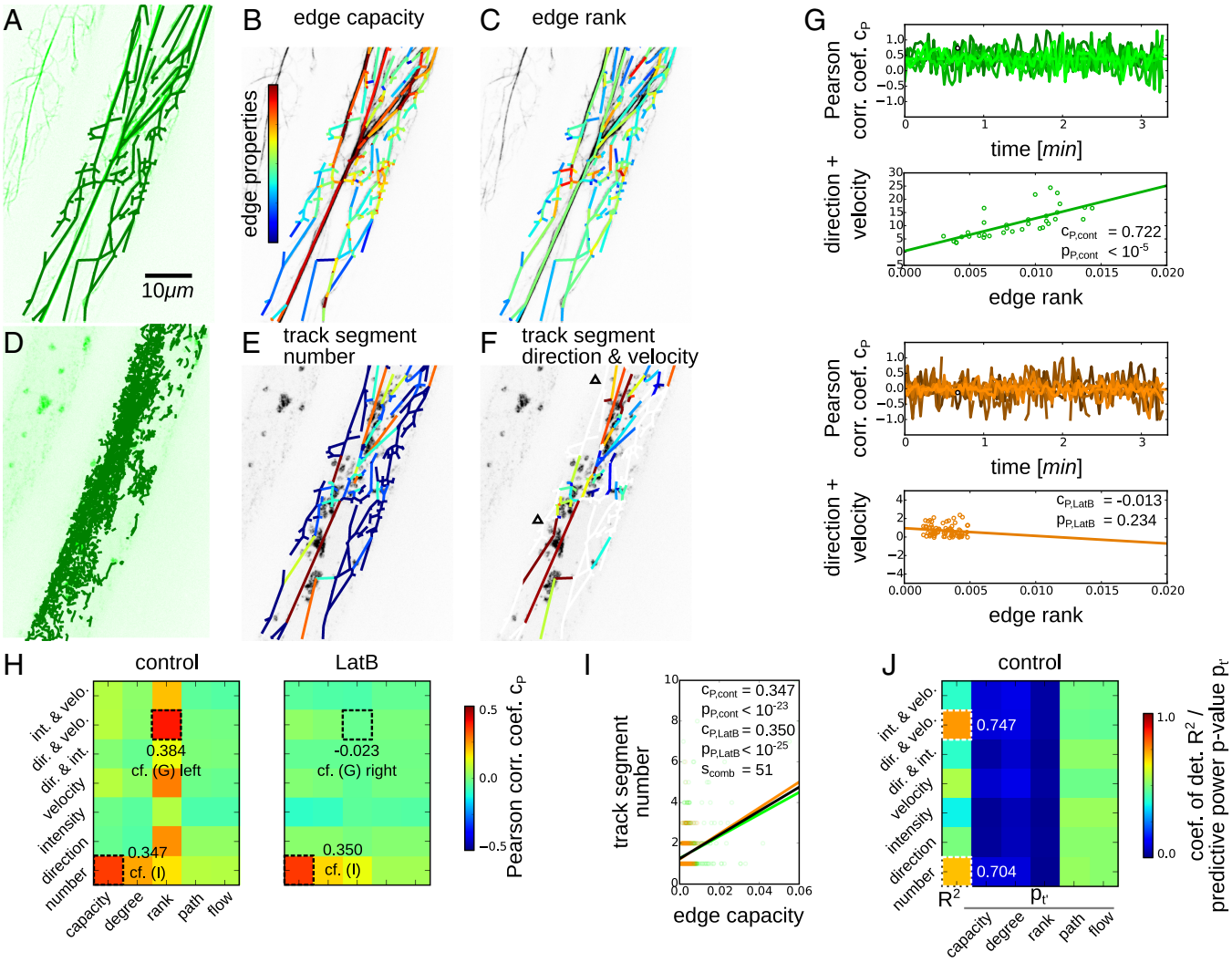

Fig. 4. Analysis of cellular organization of actin cytoskeleton enables prediction of Golgi dynamics. Shown are results for partially elongated hypocotyl cells of plants treated with the actin-disrupting drug LatB (orange) and untreated control cells (green). (*A*) Overlay of cellular recording of actin cytoskeleton and extracted actin network. (*B*) Extracted actin network with edge colors representing their capacities, i.e., average thicknesses. (*C*) Extracted actin network with edge colors representing their edge ranks. (*D*) Overlay of cellular recording of Golgi and Golgi tracks throughout the recording. (*E*) Golgi flow network with edge colors representing the numbers of close-by Golgi, i.e., track segments with starting points within 8 pixels from a given edge. (*F*) Golgi flow network with edge colors representing the direction and velocity of close-by Golgi track segments (no Golgi were assigned to white edges, e.g., triangles). (*G*) Time series of Pearson correlation coefficients c_P between Golgi track segment direction and velocity and actin edge rank (*Upper*) and exemplary scatter plots for one time point for a control and a LatB-treated cell, respectively (*Lower*; compare to open circles in *Upper*). (*H*) Heat maps of Pearson correlation coefficients c_P between different edge properties of actin and Golgi flow networks for control (*Left*) and LatB-treated (*Right*) cells. For control cells and LatB-treated cells, there was a significant correlation between the actin edge capacity and the Golgi number (compare to *I*). Correlations between the actin edge rank and Golgi direction and velocity were significant for the control cells with $c_P = 0.384$ but not for the LatB-treated cells with $c_P = -0.023$ (compare to *G*). (*I*) Scatter plots of the number of Golgi close to an edge and the respective edge capacity showed positive correlations with $c_P = 0.347$ for control and $c_P = 0.350$ for LatB-treated cells. The slope of a linear regression for the combined data was $s = 51$ (black). (*J*) Heat map of coefficients of determination R^2 for multiple linear regressions of the Golgi flow network edge properties (first column) and the respective predictive power *P* values $P_{t'}$ of the actin edge properties that were used as predictors (last five columns; one-sample two-sided *t* test *P* values $P_{t'}$ measure whether inclusion of the respective predictor improves the prediction) for the control cells. Coefficients of determination were highest for direction- and velocity-related Golgi properties ($R^2 > 0.7$). The actin capacity, degree, and rank were more reliable predictors ($P_{t'} < 0.05$) than edge flow and path betweenness ($P_{t'} \geq 0.05$).

wiggling behavior of Golgi (Fig. 3*F*) in LatB-treated cells. We further evaluated the correlations between all pairs of edge properties, averaged across the studied cells and time points (Fig. 4*H*). Some pairs of properties, such as Golgi direction and velocity and actin edge rank discussed above, were correlated for the control cells ($|c_P| > 0.2$) but not for the LatB-treated cells ($|c_P| \leq 0.2$; Fig. 4*G*). Only the number of Golgi close to a given edge was correlated with the respective edge capacity and edge degree for both control and LatB-treated cells (Fig. 4*I*). These findings show that although the flow of Golgi is severely altered by the LatB treatment, Golgi still agglomerate in the vicinity of the actin stubs (Fig. 3*I*). However, for most pairs of actin and Golgi flow network edge properties, there was no or only weak correlation ($|c_P| \leq 0.2$). Hence, whereas in particular, edge flow and path betweenness have been suggested to predict transport in real-world networks (55–57), they were not predictive of Golgi transport along the actin cytoskeleton in hypocotyl plant cells. This deviation may be due to different transport requirements in particular regions of the cell, especially during hypocotyl elongation growth (37, 58).

Because pairwise correlations were of moderate value, we then used multiple linear regression to see whether certain aspects of Golgi flow could be predicted from a combination of actin edge properties. Indeed, the number of Golgi close to an actin edge (Fig. 4*K*; coefficient of determination $R^2 = 0.704$) and the Golgi direction and velocity ($R^2 = 0.747$) were accurately predicted from the edge properties of the underlying actin cytoskeletal network. Moreover, edge capacity, edge degree, and edge rank of the actin network had higher predictive power (one-sample two-sided t test P values $P_{t'} < 0.05$ for most Golgi flow properties) than the edge path and flow betweenness ($P_{t'} \geq 0.05$). As edge capacity and edge degree reflect (semi)local actin bundling, their observed high predictive power supports the finding that actin bundling is correlated with Golgi density and velocity (Fig. S5) (10). As indicated above, the edge rank measures the (global) importance of an edge in the network context and corresponds to the probability that cargo that randomly switches between adjacent filament segments is found at the given edge, whereby thicker filaments are frequented with higher probabilities. This assumption of random movement is compatible with the wiggling of Golgi (Fig. 3).

Interestingly, these correlations between actin structures and Golgi movement were very similar for growing and fully elongated hypocotyl cells (Fig. S1). Our results were confirmed by analysis of 3D data of actin cytoskeleton and Golgi (Fig. S2). Therefore, the system-wide organization of the actin cytoskeleton in hypocotyl cells shapes, and may be used to predict, the dynamic flow of Golgi.

Finally, we note that our imaging setup captured only the outer periclinal cell side, for both 2D and 3D data. Because 3D imaging of the complete, quickly rearranging plant cytoskeleton is not yet feasible, we modeled the cylindrical geometry of the cortical cytoskeleton by periodically extending the original, 2D extracted network. Whereas cytoskeletal structures on different cell sides generally differ (e.g., refs. 59 and 60 for actin and ref. 61 for microtubules), it is parsimonious and avoids an unbiological plane-like cytoskeletal geometry. Indeed, taking into account this cylindrical geometry moderately but significantly improved the predictive power of our regression-based analyses of Golgi movement (Fig. S4). Taken together, our data show that Golgi transport in hypocotyl cells is not merely determined by the local structure of the cortical cytoskeleton, but also depends on larger architectural contexts, as well as its cylindrical geometry.

Concluding Remarks

Although the molecular details of actin monomers and filaments as well as actin-associated proteins are relatively well studied, quantifying actin-based transport in a larger cellular context remains challenging. To address this gap, we introduced an accurate image-based network representation of the actin cytoskeleton to facilitate automated and unbiased quantification of cytoskeletal phenotypes and functions. We used this framework to establish that system-level properties of the actin cytoskeleton determine key features of Golgi transport in *Arabidopsis* hypocotyl cells.

Our approach of integrating cytoskeletal network structures with tracking data of organelles is directly transferable to various biological systems and functions: In plants, in addition to the analysis of different cell types, transport of mitochondria (4, 10) and photodamage avoidance movement of chloroplasts (62) represent interesting test grounds. In animals, it has been shown that cytoplasmic streaming in fruit fly oocytes (63) and transport of lysosomes in monkey kidney cells depend on microtubules (7). Although these are interesting local correlations of cytoskeletal features and organelle transport, we expect broader, system-level understanding of these processes by the application of interdisciplinary approaches such as ours. Our automated framework paves the way for quantitative assessment of the actin cytoskeleton and trafficking in, for example, large-scale chemical and genetic screens. Moreover, our findings indicate that network-based models could be used to predict potential exchange sites of Golgi-related material. Altogether, the presented combination of experimental imaging techniques and theoretical network-based analyses provides an important step toward a systems understanding and, ultimately, control of cytoskeleton-based transport.

Materials and Methods

Plant Material and Experimental Setup. We used *Arabidopsis* Columbia-0 35S:FABD-GFP and pCesA6:tdT-CesA6 dual-labeled, 3-d-old, and dark-grown seedlings (12, 36) to study actin cytoskeleton and Golgi bodies (*SI Materials and Methods* and Movie S1). For drug and control treatment, seedlings were floated on distilled water with and without 150 nM LatB, respectively. Image series of partially elongated hypocotyl cells around 1 mm below the apical hook were captured using a spinning-disk confocal microscope with a spatial resolution of 0.133 pixel$^{-1}\cdot\mu$m and a time interval of 2 s between subsequent 2D images (64). In a slightly modified imaging setup, both growing and fully elongated cells around 1 mm and 5 mm below the apical hook, respectively, were imaged for comparison. Additionally, 3D image stacks were obtained using the same setup with 1 μm between three subsequent z slices.

Extraction and Randomization of Actin Networks. We corrected the potential drift of the seedlings using Fiji-StackReg rigid body stack registration (45, 65), compensated photobleaching by normalizing mean intensities, and improved the signal-to-noise ratio by using the Fiji-BackgroundSubtraction filter with a radius of 50 pixels (66) (*SI Materials and Methods*; see mathbiol.mpimp-golm.mpg.de/CytoSeg/ for open-source code and examples). To represent the actin cytoskeleton as a network in 2D and 3D, we enhanced filamentous structures of width v_{width} with a 2D tubeness filter (67), applied an adaptive median threshold with block size v_{thres} (68), skeletonized the resultant binary image (69), and removed all spurious connected components smaller than v_{size} pixels or with average intensities below v_{int} of the average component intensity. We identified the nodes of the network as crossings or endpoints of filaments. We added an edge between two nodes if they were directly connected by a skeleton line and assigned different edge weights such as its capacity, i.e., the average intensity along the respective filament per unit length. We gauged the four imaging parameters, using synthetic images of known cytoskeleton-like structures and manual segmentations of cytoskeleton images as a gold standard. To assess the biological relevance of the studied actin network properties, we used a first null model that distributes the nodes of the original network randomly and uniformly across the cell area (2D) or volume (3D) and shuffles edges such that their Euclidean length is preserved. A second null model shuffles only the edge properties of the original network (19).

Quantification of Golgi Movement. We automatically tracked the movement of Golgi in 2D and 3D, using Fiji-TrackMate (*SI Materials and Methods*). We detected the Golgi as particles of around 5 pixels in radius (44, 45). We then linked the Golgi in different frames, using the linear assignment problem tracker with a maximum linkage distance of 24 pixels, a maximum gap-closing distance of 24 pixels, and a maximum frame gap number of 4. To correlate actin structures with Golgi movement, we constructed auxiliary Golgi flow networks by copying the actin network. Each edge of the Golgi flow network was then assigned different weighting factors, e.g., the number of track segments within a cutoff distance of 8 pixels or the average velocity of close-by Golgi.

ACKNOWLEDGMENTS. D.B. was funded by an International Max Planck Research School scholarship. S.P. was funded by the Max Planck Society, an Australian Research Council Future Fellowship grant (FT160100218), an R@MAP Professorship at University of Melbourne, and a Dyason travel grant. S.P. and Z.N. acknowledge an International Research and Research Training Fund (Research Network and Consortia) grant.

1. Luby-Phelps K (2000) Cytoarchitecture and physical properties of cytoplasm: Volume, viscosity, diffusion, intracellular surface area. *Int Rev Cytol* 192:189–221.
2. Ellis RJ (2001) Macromolecular crowding: An important but neglected aspect of the intracellular environment. *Curr Opin Struct Biol* 11:114–119.
3. Goldstein RE, van de Meent JW (2015) A physical perspective on cytoplasmic streaming. *Interface Focus* 5:20150030.
4. Wang P, Hussey PJ (2015) Interactions between plant endomembrane systems and the actin cytoskeleton. *Front Plant Sci* 6:422.

5. Kim H, Park M, Kim SJ, Hwang I (2005) Actin filaments play a critical role in vacuolar trafficking at the Golgi complex in plant cells. *Plant Cell* 17:888–902.
6. Cheung AY, de Vries SC (2008) Membrane trafficking: Intracellular highways and country roads. *Plant Physiol* 147:1451–1453.
7. Bálint S, Verdeny Vilanova I, Sandoval Álvarez A, Lakadamyali M (2013) Correlative live-cell and superresolution microscopy reveals cargo transport dynamics at microtubule intersections. *Proc Natl Acad Sci USA* 110:3375–3380.
8. Volkmann D, Baluska F (1999) Actin cytoskeleton in plants: From transport networks to signaling networks. *Microsc Res Tech* 47:135–154.
9. Tominaga M, et al. (2000) The role of plant villin in the organization of the actin cytoskeleton, cytoplasmic streaming and the architecture of the transvacuolar strand in root hair cells of Hydrocharis. *Planta* 210:836–843.
10. Akkerman M, Overdijk EJ, Schel JH, Emons AMC, Ketelaar T (2011) Golgi body motility in the plant cell cortex correlates with actin cytoskeleton organization. *Plant Cell Physiol* 52:1844–1855.
11. Nebenführ A, et al. (1999) Stop-and-go movements of plant Golgi stacks are mediated by the acto-myosin system. *Plant Physiol* 121:1127–1142.
12. Sampathkumar A, et al. (2013) Patterning and lifetime of plasma membrane-localized cellulose synthase is dependent on actin organization in Arabidopsis interphase cells. *Plant Physiol* 162:675–688.
13. Staiger CJ, Baluška F, Volkmann D, Barlow P (2000) *Actin: A Dynamic Framework for Multiple Plant Cell Functions* (Springer, Amsterdam), 1st Ed.
14. Shimmen T, Yokota E (2004) Cytoplasmic streaming in plants. *Curr Opin Cell Biol* 16:68–72.
15. Woodhouse FG, Goldstein RE (2013) Cytoplasmic streaming in plant cells emerges naturally by microfilament self-organization. *Proc Natl Acad Sci USA* 110:14132–14137.
16. Neri I, Kern N, Parmeggiani A (2013) Modeling cytoskeletal traffic: An interplay between passive diffusion and active transport. *Phys Rev Lett* 110:098102.
17. Houtman D, et al. (2007) Hydrodynamic flow caused by active transport along cytoskeletal elements. *Europhys Lett* 78:18001.
18. Ando D, Korabel N, Huang KC, Gopinathan A (2015) Cytoskeletal network morphology regulates intracellular transport dynamics. *Biophys J* 109:1574–1582.
19. Breuer D, et al. (2014) Quantitative analyses of the plant cytoskeleton reveal underlying organizational principles. *J R Soc Interface* 11:20140362.
20. Breuer D, Nikoloski Z (2014) img2net: Automated network-based analysis of imaged phenotypes. *Bioinformatics* 30:3291–3292.
21. Yanagisawa M, et al. (2015) Patterning mechanisms of cytoskeletal and cell wall systems during leaf trichome morphogenesis. *Nat Plants* 1:15014.
22. Kitano H (2002) Systems biology: A brief overview. *Science* 295:1662–1664.
23. Gardel ML, et al. (2004) Elastic behavior of cross-linked and bundled actin networks. *Science* 304:1301–1305.
24. Banerjee N, Park J (2015) Modeling and simulation of biopolymer networks: Classification of the cytoskeleton models according to multiple scales. *Korean J Chem Engineer* 32:1207–1217.
25. Mayerich D, Bjornsson C, Taylor J, Roysam B (2012) NetMets: Software for quantifying and visualizing errors in biological network segmentation. *BMC Bioinformatics* 13:S7.
26. Xu T, et al. (2015) SOAX: A software for quantification of 3D biopolymer networks. *Sci Rep* 5:9081.
27. Clark AG, Dierkes K, Paluch EK (2013) Monitoring actin cortex thickness in live cells. *Biophys J* 105:570–580.
28. Boevink P, et al. (1998) Stacks on tracks: The plant Golgi apparatus traffics on an actin/ER network. *Plant J* 15:441–447.
29. Dupree P, Sherrier DJ (1998) The plant Golgi apparatus. *Biochim Biophys Acta* 1404:259–270.
30. Nebenführ A, Staehelin LA (2001) Mobile factories: Golgi dynamics in plant cells. *Trends Plant Sci* 6:160–167.
31. Wakatsuki T, Schwab B, Thompson NC, Elson EL (2001) Effects of cytochalasin D and latrunculin B on mechanical properties of cells. *J Cell Sci* 114:1025–1036.
32. Newman M (2009) *Networks: An Introduction* (Oxford Univ Press, Oxford), 1st Ed.
33. Claessens MM, Bathe M, Frey E, Bausch AR (2006) Actin-binding proteins sensitively mediate F-actin bundle stiffness. *Nat Mater* 5:748–753.
34. Breuer D, Nikoloski Z (2015) DeFiNe: An optimisation-based method for robust disentangling of filamentous networks. *Sci Rep* 5:18267.
35. Fu Y, Li H, Yang Z (2002) The rop2 GTPase controls the formation of cortical fine f-actin and the early phase of directional cell expansion during Arabidopsis organogenesis. *Plant Cell* 14:777–794.
36. Sheahan MB, Staiger CJ, Rose RJ, McCurdy DW (2004) A green fluorescent protein fusion to actin-binding domain 2 of Arabidopsis fimbrin highlights new features of a dynamic actin cytoskeleton in live plant cells. *Plant Physiol* 136:3968–3978.
37. Gendreau E, et al. (1997) Cellular basis of hypocotyl growth in Arabidopsis thaliana. *Plant Physiol* 114:295–305.
38. Fu Y, Wu G, Yang Z (2001) Rop GTPase–dependent dynamics of tip-localized F-actin controls tip growth in pollen tubes. *J Cell Biol* 152:1019–1032.
39. Thomas C, et al. (2009) Actin bundling in plants. *Cell Motil Cytoskeleton* 66:940–957.
40. Crowell EF, et al. (2009) Pausing of Golgi bodies on microtubules regulates secretion of cellulose synthase complexes in Arabidopsis. *Plant Cell* 21:1141–1154.
41. Tominaga M, et al. (2003) Higher plant myosin XI moves processively on actin with 35 nm steps at high velocity. *EMBO J* 22:1263–1272.
42. Paredez AR, Somerville CR, Ehrhardt DW (2006) Visualization of cellulose synthase demonstrates functional association with microtubules. *Science* 312:1491–1495.
43. Luo Y, et al. (2015) V-ATPase activity in the TGN/EE is required for exocytosis and recycling in Arabidopsis. *Nat Plants* 1:15094.
44. Jaqaman K, et al. (2008) Robust single-particle tracking in live-cell time-lapse sequences. *Nat Methods* 5:695–702.
45. Schindelin J, et al. (2012) Fiji: An open-source platform for biological-image analysis. *Nat Methods* 9:676–682.
46. Viswanathan GM, et al. (1999) Optimizing the success of random searches. *Nature* 401:911–914.
47. Humphries NE, Weimerskirch H, Queiroz N, Southall EJ, Sims DW (2012) Foraging success of biological Lévy flights recorded in situ. *Proc Natl Acad Sci USA* 109:7169–7174.
48. Matthäus F, Jagodic M, Dobnikar J (2009) E. coli superdiffusion and chemotaxis-search strategy, precision, and motility. *Biophys J* 97:946–957.
49. Clauset A, Shalizi CR, Newman M (2009) Power-law distributions in empirical data. *SIAM Rev* 51:661–703.
50. Zhao K, et al. (2015) Optimal Lévy-flight foraging in a finite landscape. *J R Soc Interface* 12:20141158.
51. Sutantyo DK, Kernbach S, Levi P, Nepomnyashchikh VA (2010) Multi-robot searching algorithm using Lévy flight and artificial potential field. *IEEE SSRR* 1:1–6.
52. Viswanathan GM, Da Luz MG, Raposo EP, Stanley HE (2011) *The Physics of Foraging: An Introduction to Random Searches and Biological Encounters* (Cambridge Univ Press, New York), 1st Ed.
53. Hills TT, Kalff C, Wiener JM (2013) Adaptive Lévy processes and area-restricted search in human foraging. *PLoS One* 8:e60488.
54. Buchnik L, Abu-Abied M, Sadot E (2014) Role of plant myosins in motile organelles: Is a direct interaction required? *J Integr Plant Biol* 57:23–30.
55. Borgatti SP (2005) Centrality and network flow. *Soc Networks* 27:55–71.
56. Jiang B, Zhao S, Yin J (2008) Self-organized natural roads for predicting traffic flow: A sensitivity study. *J Stat Mech* 2008:P07008.
57. Kazerani A, Winter S (2009) Can betweenness centrality explain traffic flow? *Proceedings of the 12th AGILE International Conference on Geographic Information Science*, eds Sester M, Bernard L, Paelke V (Leibniz Universität Hannover, Hannover, Germany), pp 1702–1717.
58. Geisler DA, Sampathkumar A, Mutwil M, Persson S (2008) Laying down the bricks: Logistic aspects of cell wall biosynthesis. *Curr Opin Plant Biol* 11:647–652.
59. Jacques E, Verbelen JP, Vissenberg K (2014) Review on shape formation in epidermal pavement cells of the Arabidopsis leaf. *Funct Plant Biol* 41:914–921.
60. Armour WJ, Barton DA, Law AM, Overall RL (2015) Differential growth in periclinal and anticlinal walls during lobe formation in Arabidopsis cotyledon pavement cells. *Plant Cell* 27:2484–2500.
61. Peaucelle A, Wightman R, Höfte H (2015) The control of growth symmetry breaking in the Arabidopsis hypocotyl. *Curr Biol* 25:1746–1752.
62. Kasahara M, et al. (2002) Chloroplast avoidance movement reduces photodamage in plants. *Nature* 420:829–832.
63. Ganguly S, Williams LS, Palacios IM, Goldstein RE (2012) Cytoplasmic streaming in Drosophila oocytes varies with kinesin activity and correlates with the microtubule cytoskeleton architecture. *Proc Natl Acad Sci USA* 109:15109–15114.
64. Sampathkumar A, et al. (2011) Live cell imaging reveals structural associations between the actin and microtubule cytoskeleton in Arabidopsis. *Plant Cell* 23:2302–2313.
65. Thévenaz P, Ruttimann UE, Unser M (1998) A pyramid approach to subpixel registration based on intensity. *IEEE Trans Image Process* 7:27–41.
66. Sternberg SR (1983) Biomedical image processing. *IEEE Comput Soc* 16:22–34.
67. Sato Y, et al. (1998) Three-dimensional multi-scale line filter for segmentation and visualization of curvilinear structures in medical images. *Med Image Anal* 2:143–168.
68. van der Walt S, et al. (2014) scikit-image: Image processing in Python. *PeerJ* 2:e453.
69. Haralick RM, Sternberg SR, Zhuang X (1987) Image analysis using mathematical morphology. *IEEE Trans Pattern Anal Mach Intell* 4:532–550.
70. van Rossum G, Drake FL (2011) *Python Language Reference Manual* (Network Theory, Godalming, UK), 1st Ed.
71. Dhondt S, et al. (2012) Quantitative analysis of venation patterns of Arabidopsis leaves by supervised image analysis. *Plant J* 69:553–563.
72. Baumgarten W, Hauser MJ (2012) Computational algorithms for extraction and analysis of two-dimensional transportation networks. *J Comput Interdiscip Sci* 3:107–16.
73. Cooper GM (2000) *The Cell: A Molecular Approach* (ASM, Boston), 2nd Ed.
74. Dirnberger M, Kehl T, Neumann A (2014) NEFI: Network extraction from images. *Sci Rep* 5:15669.
75. Obara B, Grau V, Fricker MD (2012) A bioimage informatics approach to automatically extract complex fungal networks. *Bioinformatics* 28:2374–2381.
76. Obara B, Fricker M, Gavaghan D, Grau V (2012) Contrast-independent curvilinear structure detection in biomedical images. *IEEE Trans Image Process* 21:2572–2581.
77. Mayerich DM, Keyser J (2008) Filament tracking and encoding for complex biological networks. *Proceedings of the 2008 ACM Symposium on Solid and Physics Modeling*, eds Haines E, McGuire M (ACM, New York), pp 353–358.
78. Meijering E (2010) Neuron tracing in perspective. *Cytometry A* 77:693–704.
79. Caldarelli G, Capocci A, De Los Rios P, Munoz MA (2002) Scale-free networks from varying vertex intrinsic fitness. *Phys Rev Lett* 89:258702.
80. Cover TM, Hart PE (1967) Nearest neighbor pattern classification. *IEEE Trans Inf Theory* 13:21–27.
81. Belsley DA (2006) *Encyclopedia of Statistical Sciences* (Wiley Online Library, Bethesda), 2nd Ed.
82. Dijkstra EW (1959) A note on two problems in connexion with graphs. *Numer Math* 1:269–271.
83. Berger F, Keller C, Klumpp S, Lipowsky R (2015) External forces influence the elastic coupling effects during cargo transport by molecular motors. *Phys Rev E* 91:022701.
84. Klumpp S, Lipowsky R (2005) Cooperative cargo transport by several molecular motors. *Proc Natl Acad Sci USA* 102:17284–17289.
85. Staiger CJ, et al. (2009) Actin filament dynamics are dominated by rapid growth and severing activity in the Arabidopsis cortical array. *J Cell Biol* 184:269–280.